scientific reports

Check for updates

OPEN

Evaluation of hydrogen production via steam reforming and partial oxidation of dimethyl ether using response surface methodology and artificial neural network

Karim Mansouri, Fatemeh Bahmanzadegan & Ahad Ghaemi✉

This study aims to develop two models for thermodynamic data on hydrogen generation from the combined processes of dimethyl ether steam reforming and partial oxidation, applying artificial neural networks (ANN) and response surface methodology (RSM). Three factors are recognized as important determinants for the hydrogen and carbon monoxide mole fractions. The RSM used the quadratic model to formulate two correlations for the outcomes. The ANN modeling used two algorithms, namely multilayer perceptron (MLP) and radial basis function (RBF). The optimum configuration for the MLP, employing the Levenberg–Marquardt (trainlm) algorithm, consisted of three hidden layers with 15, 10, and 5 neurons, respectively. The ideal RBF configuration contained a total of 80 neurons. The optimum configuration of ANN achieved the best mean squared error (MSE) performance of 3.95e−05 for the hydrogen mole fraction and 4.88e−05 for the carbon monoxide mole fraction after nine epochs. Each of the ANN and RSM models produced accurate predictions of the actual data. The prediction performance of the ANN model was 0.9994, which is higher than the RSM model's 0.9771. The optimal condition was obtained at O/C of 0.4, S/C of 2.5, and temperature of 250 °C to achieve the highest H_2 production with the lowest CO emission.

Keywords Hydrogen production, Dimethyl ether, Steam reforming, Partial oxidation, Response surface methodology (RSM), Artificial neural network (ANN)

List of symbols

b	Bias (–)
C_i	Center point (–)
f	Function
Φ_i	Gaussian function
i	Number of neurons in the hidden layer
N	Number of data sets for training (–)
n	Neurons
R^2	Correlation coefficient (%)
W	Weight factor (–)
W_{ij}	Weight-related to each hidden neuron (–)
x_i	Input examples (attributes)
Y	Output vector (–)
y_j	Target output
y_{H_2}	H_2 mole fraction
y_{CO}	CO mole fraction

School of Chemical, Petroleum and Gas Engineering, Iran University of Science and Technology, Narmak, Tehran 16846, Iran. ✉email: aghaemi@iust.ac.ir

Greek symbols

α	Constants in turbulence models (–)
β	Interaction coefficient
γ_{jk}	Neuron j's output from k's layer
σ_i	Spread of Gaussian function (–

Abbreviations

AARD	Average absolute relative deviation (%)
ANN	Artificial neural networks
MAE	Mean absolute error
MAPE	Mean absolute percentage error
MSE	Mean square error
S/C	Steam/carbon
O/C	Oxygen/carbon

Terminology

Neurons	Neurons are the basic units of the large neural network
Bias	Bias is a constant that helps the model fit the given data best
Activation function	The activation function is a mathematical function between the input feeding current neuron and its output going to the next layer
Weight	Represents the importance and strengths of the feature/input to the neurons
Epoch	In the training process, the inputs enter each training step and give an output compared with the target to calculate an error. This process calculates and modifies weights and biases in each epoch

Global population expansion and urbanization have led to enormous increases in energy demand, primarily reliant on fossil fuels. This has resulted in higher quantities of CO_2 and other greenhouse gases (GHGs), causing global warming. Therefore, decarbonizing the energy supply with clean, sustainable, and renewable energy is vital for long-term viability and global safety[1,2]. Hydrogen has garnered significant interest among several alternative fuels as a prospective clean energy source. Hydrogen, unlike fossil fuels, is not easy to find in nature. On the other hand, it can be made from any main energy source and used as fuel in either an internal combustion engine or a fuel cell. It just generates water as a byproduct. Hydrogen is the only known fuel that doesn't contain carbon and has the highest energy density of any known fuel. Because of this, it is widely seen as an environmentally friendly alternative to fossil fuels. Another benefit is that hydrogen can be used at home with the right storage technologies. This is because normal methods can safely transport it, and it can be stored as either a compressed gas, a cryogenic liquid, or a solid hydride[3,4]. The investigation of discernible sustainable hydrogen sources from various feedstocks, namely methanol, ethanol, and dimethyl ether (DME), presented in Table 1, unveiled a notable limitation: the temperatures essential for hydrogen production from methanol and ethanol were considerably elevated compared to those necessary for employing DME. In addition, dimethyl ether (DME) is a promising fuel for generating hydrogen-rich fuel cells due to its high hydrogen-to-carbon ratio, high energy density, and non-toxic properties. As with liquefied petroleum gas (LPG), it can be easily handled, stored, and transported, and LPG's equipment can be easily adapted for DME due to its similar physical properties[5]. DME has lower NO_x and SO_x pollutants than traditional diesel and is non-carcinogenic, non-teratogenic, and non-mutagenic. It burns with a visible blue flame and produces the least greenhouse gas (GHG) emissions compared to other fuels. It has the highest well-to-wheel efficiencies of all non-petroleum-based fuels using conventional, hybrid, and fuel processor fuel cell vehicle technologies[6]. Furthermore, regarding economic viability and thermodynamic preference, the direct conversion of syngas into DME is superior to the synthesis of methanol[7]. There are three primary processes for the production of hydrogen-rich fuel cell feeds using DME: steam reforming (SR), partial

Researcher	Catalyst	BET (m^2/g)	T(°C)	Conversion			H_2 Yield	References
				DME	Ethanol	Methanol		
Takeishi et al	γAl_2O_3(Sol)//CuZn(9 wt.%)/SiO_2(Sol) (Two-layer type)	368	300	58.6	–	–	27.2	10
Takeishi et al	γAl_2O_3(Sol)&CuZn(9–1wt.%)/SiO_2(Sol) (Mixed type)	368	300	88.4	–	–	76.6	10
Takeishi et al	Cu–Zn(4.5–0.5 wt.%)/Al_2O_3(Sol) (Single-use type)	237	300	91.9	–	–	88.8	10
Wang et al	15 wt.% Ni/zeolite	–	550	–	100	–	76.0	13
Musso et al	15 wt.% Ni/Y-ZrO_2	–	650	–	100	–	91.0	14
Prasongthum et al	10 wt.% Ni/CNTs–SF	–	–	–	100	–	40.0	15
Lorenzut et al	Ni/Cu/ZnO/Al_2O_3	–	350	–	–	100	83.0	16
Qi et al	NiAl-LDH (Ni/Al = 4.9)	–	390	–	–	94.6	70.0	17

Table 1. Several studies have been done on the optimization of hydrogen production from steam reforming.

oxidation (PO), and auto-thermal reforming (ATR)[8]. Most research papers primarily concentrate on SR, whereas there are a limited number of articles that specifically address PO and ATR[9]. Takeishi et al. investigated various copper-alumina catalysts for generating hydrogen from dimethyl ether (DME). Among these catalysts, the Cu–Zn (29–1 wt%)/Al_2O_3 catalyst exhibited the highest hydrogen production and the lowest CO production from DME. When subjected to DME steam reforming at 275 °C, the catalyst achieved a DME conversion rate of 95%, an H_2 yield of 95%, and a CO concentration of 0.8% mol[10]. However, the operational cost may increase because the SR is an endothermic process and requires a significant amount of energy. Catalytic PO is an exothermic reaction that can be coupled with an endothermic reaction to produce a valuable product. The catalytic PO's exothermic properties enable the utilization of a more compact reactor design and accelerate the initiation of reactions, presenting an encouraging advancement in technology[9,11].

For specific requirements, the combined process can be optimized through the modification of operational conditions. Combining the SR and PO processes to generate hydrogen-rich fuel cell feeds with DME gives more control over the hydrogen-to-CO (H_2/CO) ratio, which leads to a higher hydrogen yield compared to using just one process (Fig. 1). The increased fraction of fully oxidized DME also helps lower the amount of carbon monoxide (CO), which improves the performance of fuel cells[11,12].

Operating auto thermally, the energy sufficient to propel the SR reaction is provided by the PO reaction. The highest efficiency for hydrogen production is achieved through SR, whereas complete oxidation results in zero efficiency. As the process shifts from pure SR to oxidation, the production efficiency of hydrogen and the amount of CO decrease. The global minimum of CO is achieved with full oxidation, although this approach is not feasible when the intended outcome is hydrogen. If only heat energy is required, complete oxidation can be employed for rapid heating. However, for the purpose of hydrogen production, the local minimum of CO ensues under the particular conditions of pure steam reforming. Optimal processing conditions for hydrogen production efficiency, CO reduction, and total energy efficiency occur in the zone between PO and SR under steady-state conditions and without sudden heating[18].

The integration of RSM and ANN in the optimization of hydrogen production through DME steam reforming and partial oxidation indeed holds significant promise for enhancing efficiency and sustainability in various industries. By leveraging these advanced modeling and optimization techniques, researchers can effectively fine-tune the process parameters involved in DME steam reforming and partial oxidation to achieve optimal hydrogen yields while simultaneously minimizing energy consumption and environmental impact. RSM provides a systematic and efficient approach for exploring the relationship between input variables (such as temperature, pressure, and catalyst composition) and the output response (hydrogen yield). Through the design and analysis of experiments, RSM enables the generation of response surfaces that depict the relationship between the input variables and the desired output, guiding the search for optimal operating conditions. The combined use of RSM and ANN allows for a comprehensive optimization strategy, wherein Design Expert guides the experimental design and data collection process, while ANN aids in model development and prediction. Pardo et al. investigated methods to enhance the operational performance of a real steam reforming plant, with a specific focus on increasing hydrogen production or maximizing factory profits. In their study, they constructed a holistic model of the SR plant comprising seven multilayer perceptrons (MLPs) and utilized genetic algorithm (GA) and memetic algorithm (MA) optimization techniques to refine model input[19]. Zhang et al. have designed an optimal model predictive control strategy for hydrogen production. This study involves a thermodynamic assessment of hydrogen production through low-temperature auto-thermal reforming (ATR) of DME. The experimental and simulated demonstrations of the Pd/Zn/γ-Al_2O_3 catalyst, which is applied to honeycomb cordierite ceramic, revealed its effectiveness at 400 °C[20]. Chen et al. conducted a study where they utilized ANN to forecast methanol conversion and H_2 yield by incorporating input variables such as the steam-to-carbon (S/C) ratio, gas hourly space velocity (GHSV), and reaction temperature[21]. Lghalo et al. explored the thermodynamic analysis of dimethyl ether (DME) steam reforming in conjunction with a statistical approach. Employing Response Surface Methodology (RSM), they investigated potential interactions among various process factors. They developed regression models to forecast the percentage molar yield of each species, considering key factor ranges such as temperature (450–750 °C), pressure (1–5 atm), and steam-to-carbon (S/C) ratio (1–5)[22].

Previous studies (Table 2) in the literature have separately investigated the SR and PO processes, but the application of RSM and ANN to optimize hydrogen production via DME steam reforming and partial oxidation has not been explored. This research aims to utilize RSM and ANN, such as the multi-layer perceptron (MLP)

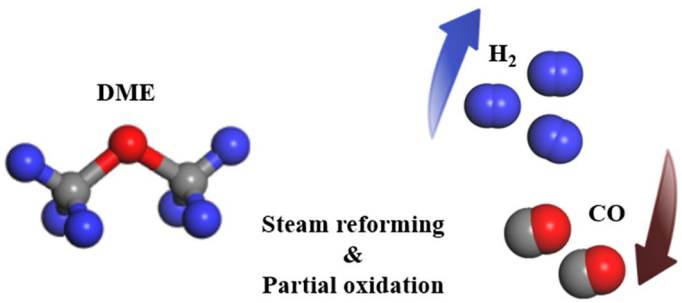

Figure 1. H_2 production from DME SR and PO.

Researcher	GHSV-1 (h^{-1})	T (°C)	P (bar)	O/C	S/C	H_2 yield R^2 (RSM)	H_2 yield R^2 (ANN)	References
Pardo et al	–	423.9–455	–	–	2.74–4	–	0.9848	[19]
Chen et al	15,000–30,000	180–280	–	–	1.5–2–2.5	0.9842	0.99	[21]
Ighalo et al	–	450–750	1–5	–	1–5	0.9914	–	[22]

Table 2. Utilizing simulations and optimization techniques to enhance hydrogen production via DME steam reforming.

and radial basis function (RBF) network approaches, to model thermodynamic data on hydrogen production from the combined processes of DME SR and PO.

However, this research has specifically concentrated on optimizing the integration of these two processes to achieve maximum H_2 production and minimize CO production. The independent variables considered include the oxygen-to-carbon ratio (O/C), steam-to-carbon ratio (S/C), and temperature (T), with the hydrogen mole fraction (y_{H_2}) and CO mole fraction (y_{CO}) as the response of the modeling approach. The impact of operating pressure on hydrogen content is found to be minimal, so all computations are conducted under atmospheric pressure conditions ($P = 1$ atm). The RSM modeling method aims to find the best conditions and create a semi-empirical model that fits the data best by looking at how different variables affect y_{H_2} and y_{CO}. In the same way, the ANN approach aims to determine the best network configuration and the most appropriate weights and biases for examining the correlation between y_{H_2} and y_{CO} and the independent variables by determining the network's specifications, such as hidden layer size, number of neurons, and training functions for the MLP network and the number of neurons, spread value, and epoch for the RBF network. The study also shows how design and statistical models can make the process more efficient. The RSM method uses thermodynamic data to fit a quadratic model, and the ANN method develops models based on thermodynamic data and does sensitivity analysis to see which input parameters are most important. The correlations facilitate the timely estimation of process yield, thereby influencing the selection of various design alternatives. Moreover, they bear significance in budgeting, forecasting, and other facets of process design and economics.

Methodology

Thermodynamic equilibrium calculations

The selected reactions for each of the exothermic and endothermic steps based on the combined mechanism of DME SR and PO for the primary thermodynamic equilibrium calculations are listed in Table 3:

After selecting reactants, products, and operating conditions (i.e., the O/C ratio, S/C ratio, and temperature), equilibrium compositions were calculated through the minimization of Gibb's free energy, using the Peng-Robinson equation as the equation of state and Aspen Tech software for multicomponent equilibria. The equilibrium compositions were subsequently charted for various processing conditions to ascertain the most favorable processing temperature and feed composition[18].

Data collection

The data required to train and test the models was gathered from previous studies in the literature[12], as this study is exclusively computational. A total of 624 data points were collected from the literature (supplementary Table S2). Out of them, 591 were utilized for training and 33 for testing. Table 4 presents some of the thermodynamic data points that pertain to the mole fraction of hydrogen and CO under different operating conditions.

RSM theory

Experimental design is a scientific methodology that entails manipulating input variables to acquire knowledge about the process and establish a desired input–output correlation. This approach has multiple advantages, including the ability to identify the pivotal aspects that impact the process, decrease the process's expenses, construct a model of the process, and ascertain the correlation between input and output variables[23]. RSM is a statistical modeling technique that uses quantitative data from well-designed experiments to answer numerous regression equations simultaneously[24]. It models the correlation between independent and dependent variables as a surface[25]. The model aims to establish a relationship, even approximate, between Y and control variables, determine the significance of factors represented by x_1, x_2,…, x_k through hypothesis testing, and determine the

Reaction	Equation	$\Delta H°_{rxn}$ (kJmol – 1)
DME PO	$CH_3OCH_3 + 0.5O_2 \rightleftharpoons 2CO + 3H_2$	− 25
DME oxidation:	$CH_3OCH_3 + 3O_2 \rightleftharpoons 2CO_2 + 3H_2O(v)$	− 1316
DME SR	$CH_3OCH_3 + 3H_2O(v) \rightleftharpoons 2CO_2 + 6H_2$	+ 135
Water–gas shift	$H_2 + CO_2 \rightleftharpoons H_2O(v) + CO$	+ 41

Table 3. Selected reactions for each step of the process.

Operating conditions			Mole fraction	
O/C	S/C	T (°C)	H_2	CO
0.40	2.50	300	0.4375	0.0071
2.00	0.75	500	0.1265	0.0160
0.00	1.25	200	0.7246	0.0693
0.80	1.50	500	0.3516	0.0475
1.20	2.50	400	0.2388	0.0081
1.60	1.50	500	0.1816	0.0179
1.60	3.00	600	0.1494	0.0151
0.40	1.50	300	0.5154	0.0223
2.40	2.25	400	0.0646	0.0018
0.80	0.50	300	0.4100	0.0679

Table 4. Some thermodynamic data are used for RSM and ANN modeling [17].

optimal settings for maximum or minimum response in a specific region[26]. Equation 1 represents the quadratic model in the RSM method.

$$Y = \beta_0 + \sum_{j=1}^{k} \beta_j x_j + \sum_{j=1}^{k} \beta_{jj} x_j^2 + \sum_{i} \sum_{j>=2}^{k} \beta_{ij} x_i x_j + e_i \quad (1)$$

where the predicted response is denoted as Y (i.e., the mole fraction of hydrogen or CO); x_i and x_j are independent variables (i and j vary from 1 to k); β_0 is the model intercept coefficient; The interaction coefficients for the linear, quadratic, and second-order terms are represented as β_j, β_{jj}, and β_{ij}, respectively; k is the number of independent parameters; whereas e_i is the error[27]. In the RSM method, the experimental data is used to fit the quadratic model described in Eq. (1), and the coefficients of the model are determined. The accuracy of the resulting model is assessed through an analysis of variance (ANOVA), the correlation coefficient (R^2), and the model's p-value. Table 5 summarizes the values of the independent parameters, organized according to their symbol assignment, response, and trial range.

ANN theory

The ANN method has become more popular over the last two decades because it seeks to model computer networks like the way the human brain and nerves are structured. Mathematicians and computer scientists created ANNs to imitate real-world neural networks. ANNs are mathematical tools or computational models that process information using a connectionist approach. They offer advantages such as high processing speed, input–output data connection, network compatibility, noisy data response, parallel processing ability, fault tolerance, and learning. ANN is typically an adaptive system that can learn from available data and map input parameters to output parameters without knowing the complex relationship between them. This adaptability is accomplished by changing the structure of the system in response to external or internal information acquired during the learning phase. Modern statistical data models use non-linear neural networks. They are frequently used to simulate complicated input–output interactions or uncover data patterns[28,29]. ANNs, consisting of three layers: input, hidden, and output, are created by interconnected neurons. The structure of these networks is determined by weight parameters and activation functions. Throughout the learning process, a dedicated training algorithm optimizes weights and bias values, aiming to minimize error values between real parameter values and the projected values by the ANN[23,30]. Neurons are the tiniest units that process data. A cell gathers information from several sources. The inputs (x_i) are multiplied by their corresponding weights (w_i), the resulting values are summed, and the bias vector (b) is added to the overall sum. This process for input data is summarized in Eq. (2).

Parameters	Type	Units	Symbol	Ranges
Oxygen-to-carbon ratio (O/C)	Input	–	A	0–2.8.0
Steam-to-carbon ratio (S/C)	Input	–	B	0.25–4.0
Temperature (T)	Input	℃	C	100–600
Hydrogen mole fraction (y_{H_2})	Response	–	y_{H_2}	0.007–0.7246
Carbon monoxide mole fraction (y_{CO})	Response	–	y_{CO}	0–0.3333

Table 5. The hydrogen production process parameters and responses.

$$net = \left(\sum_{i=1}^{n} w_i x_i\right) + b \tag{2}$$

This process ends with the results fed into a transfer function (f), and the output values (y) are derived from the following equation[31].

$$y = f(net) \tag{3}$$

In order to get acceptable outcomes from the neural network, it is important to normalize the data. To achieve this objective, all data have been normalized within the range of 0 to + 1 using Eq. (4):

$$\mathrm{X_{norm}} = \frac{2X - X_{Max} - X_{Min}}{X_{Max} - X_{Min}} \tag{4}$$

where $\mathrm{X_{norm}}$ represents the normalized data, X is the input variable, and $X_{\max}$ and $X_{\min}$ correspond to the maximum and minimum values of the data, respectively[32]. To determine network parameter values, the projected network error should be kept to a minimum for every step of the mean square error (MSE) in every iteration during network training. MSE, mean absolute error (MAE), mean absolute percentage error (MAPE), the square of the correlation coefficient (R^2), and the average absolute relative deviation (AARD%) are used to compare the model results to the validation dataset. R^2 close to 1 and near-zero MSE, MAE, and MAPE values imply network accuracy. MSE, MAE, MAPE, R^2, and AARD are obtained as follows[32–34]:

$$MSE = \frac{1}{n}\sum_{i=1}^{n}\left(Y_{predicted} - Y_{actual}\right)^2 \tag{5}$$

$$MAE = \frac{1}{n}\sum_{i=1}^{n}\left|Y_{actual} - Y_{predicted}\right| \tag{6}$$

$$MAPE = \frac{100}{n}\sum_{i=1}^{n}\frac{\left|Y_{actual} - Y_{predicted}\right|}{Y_{actual}} \tag{7}$$

$$R^2 = \frac{\sum_{i=1}^{n}\left(Y_{predicted} - Y_{actual}\right)^2}{\sum_{i=1}^{n}\left(Y_{predicted} - Y_{mean}\right)^2} \tag{8}$$

$$\mathrm{AARD} = \frac{1}{n}\sum_{i=1}^{n}\left|\frac{Y_{actual} - Y_{predicted}}{Y_{actual}}\right| \times 100 \tag{9}$$

where $Y_{predicted}$, Y_{actual}, Y_{mean}, and n denote the predicted Y value using a neural network, the actual Y value, the average Y value, and the number of data points, respectively.

MLP model

MLP is a type of neural network composed of numerous layers of simple, two-state, sigmoid processing components (nodes) or neurons that interact with one another through weighted connections. Following a lowermost input layer, there are normally several intermediate or hidden layers, followed by a top output layer. Nevertheless, every neuron within a layer is intricately linked to the neurons in adjacent layers. There are no connections between elements in a single layer. Weights determine the extent of interaction among the activity levels of interconnected neurons[35]. MLP uses the backpropagation method as a feed-forward neural network, whereby the errors are propagated backward to modify the weights and arrange data into appropriate outputs. It is a more advanced variant of the standard linear perceptron that can gather information from non-linearly separable input[36]. Based on the chosen training algorithm, weights and bias values are adjusted in each epoch, attaining optimal weight and bias values. The selection of the number of hidden layers and neurons in the MLP network is done through trial and error. By evaluating the MSE values, it is possible to determine the network's optimal structure by adjusting the number of neurons and the size of the hidden layers[37]. The computational basis of the MLP network is expressed in Eq. (10).

$$y = f_2\left(\sum_{j=1}^{n} w_j f_1\left(\sum_{i=1}^{n} h_{ij} x_i + b_j\right) + b_0\right) \tag{10}$$

The weight matrix, bias vector, and activation function of the hidden layer are denoted as h_{ij}, b_j, and f_1, respectively. Similarly, the weight, bias vector, and activation function of the output layer are represented as w_j, b_0, and f_2[38]. The structure of an MLP with three hidden layers is depicted in Fig. 2. During the training phase of the network, the objective is to minimize MSE by producing an error signal derived from the activation function. Subsequently, the weights are then adjusted by propagating this error signal backward through the layers. Weights that lower MSE are preferable.

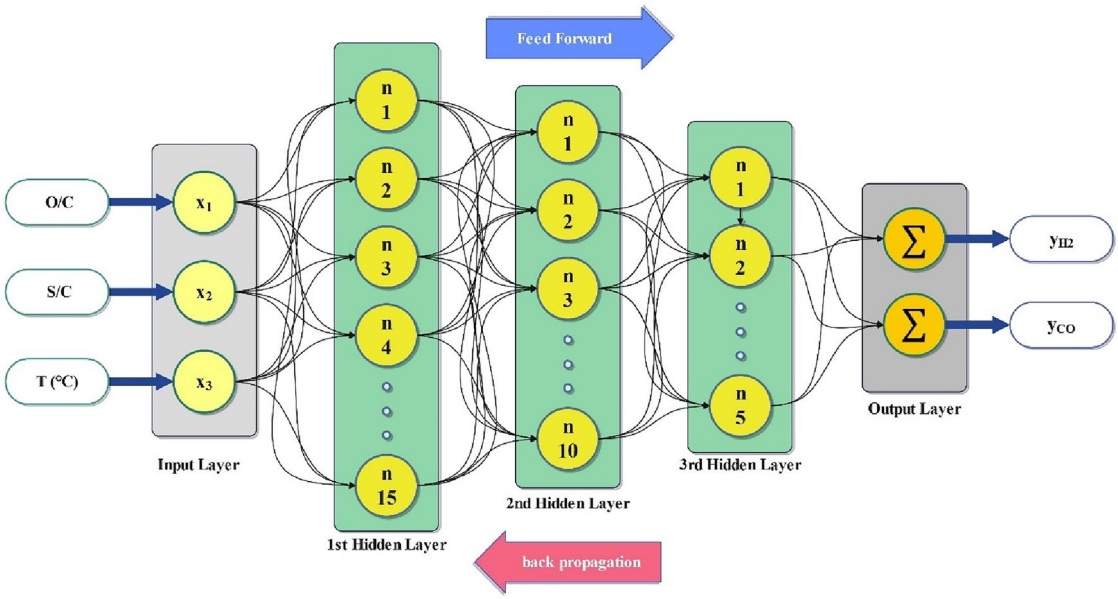

Figure 2. Schematic diagram of the MLP network with three hidden layers.

RBF model

RBF networks have been demonstrated to be general approximates of a subclass of single-hidden-layer feedforward neural networks[39]. This network, developed by Broomhead and Lowe, is widely used in complex dynamic system modeling based on its exceptional capabilities for nonlinear mapping, self-organization, generalization, and self-learning[40]. The RBF network is composed of three layers: the input layer, the hidden layer, and the output layer. The input layer is tasked with processing a substantial quantity of non-linear data, which is then sent to the hidden layer[41]. The hidden layer contains a variety of neurons, and the optimal number of neurons is determined by trial and error. The basic concept of the learning process of these networks is to minimize the MSE until it reaches a certain value (e.g., 0.0001) or a specified number of epochs (e.g., 100 epochs)[42]. In the RBF network, the Gaussian function, defined by Eq. (11), is the most commonly utilized activation function for processing data.

$$\Phi_i(x - C_i \times b) = exp\left(-\frac{(x - C_i \times b)^2}{2\sigma_i^2}\right) \tag{11}$$

where x is the input variable, c_i is the center point, b is the bias, and σ_i is the spread of the Gaussian function[43], and Eq. (12) shows the general form of the computation basis in the RBF network.

$$y = \sum_{i=1}^{n} w_i \Phi_i \tag{12}$$

where the output of the network is denoted by y, the Gaussian function is represented by Φ_i, the number of hidden layer neurons is indicated by n, the linkage weight between the i neuron and the output layer is represented by w_i, and the || shows the Euclidean norm[44]. Figure 3 shows the structure of the RBF network with a single hidden layer used in this work.

ANN structure design

A flowchart illustrating the ANN model design procedure is shown in Fig. 4. In the first step, we gather data from the literature. The thermodynamic and process parameters such as S/C, O/C, and temperature were used as input data, and y_{H_2} or y_{CO} were employed as output data. In the next step, the model is created by defining the input and output elements. Following that, the input and output data were normalized before selecting the learning algorithm for developing the network structure. In the subsequent stage, the ANN model training approach and network training validation are used to match the data and set the training, which includes adjusting the inputs and outputs of the network. The chosen model is trained using a certain data set to maximize its performance by adjusting network parameters such as weight, bias, or threshold. The network validation data is supplemented by including a specific dataset during the training phase, whereas the network testing is performed using the selected test data. Once generalizations have been optimized, the training process is complete. To evaluate the accuracy of the trained model, statistical metrics such as R^2 value and MSE were used to compare the model's predictions with the actual data. The MLP model's optimum configuration was discovered by variation with different numbers of hidden layers, neurons within each layer, and network training algorithms to get the most accurate predictions. In contrast, the RBF network typically determines the number of neurons by an iterative process of trial and error. Initially, many neurons are used in the single hidden layer, and then the number is gradually reduced until

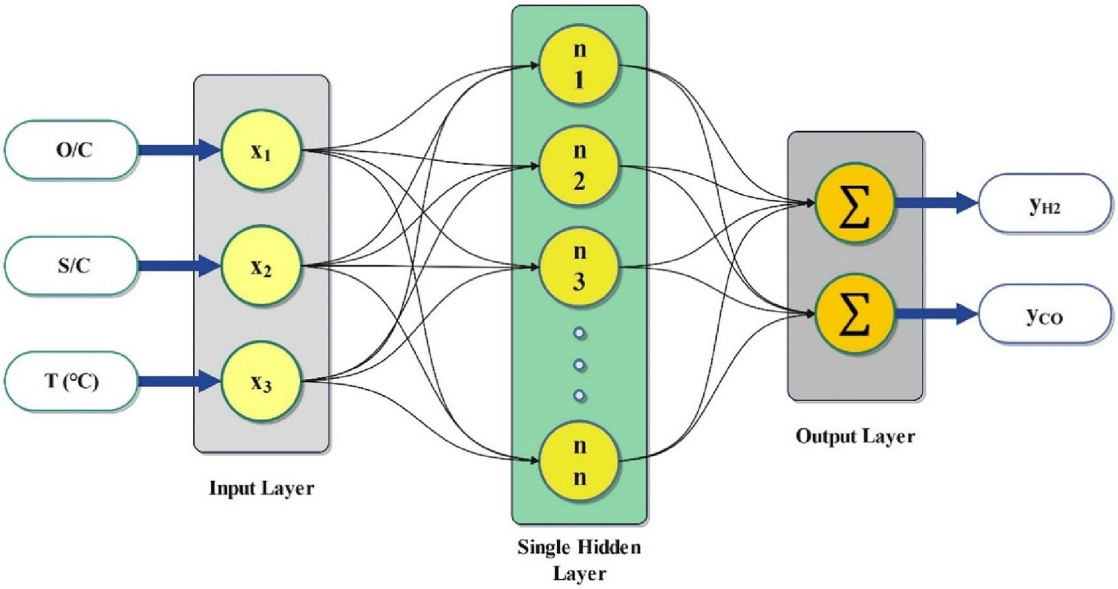

Figure 3. Schematic diagram of the RBF network with a single hidden layer.

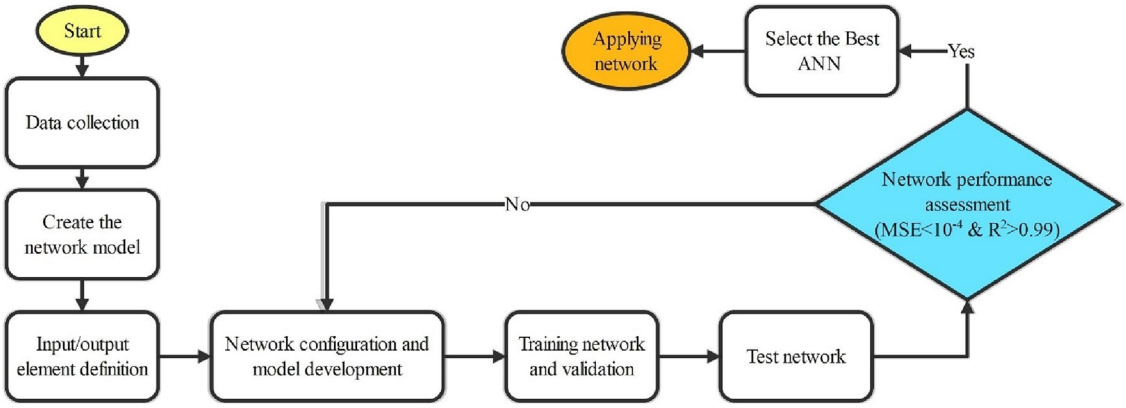

Figure 4. Schematic flowchart of ANN structure design.

the least MSE is achieved. The decrease in the number of neurons leads to a reduction in the proportional error. The algorithm's training procedure ends upon achieving the optimized error from the testing data.

Result

RSM results

This section analyzes several fitting models and their ability to match thermodynamic data. Based on its optimum R^2 value, the quadratic model without a transfer function was selected as the most accurate model. In addition, the dependence of hydrogen production on variable parameters and RSM-based optimization of hydrogen production were discussed.

Analysis of variance (ANOVA)

The ANOVA results from the thermodynamic data analysis are shown in Table 6. The F-value determines the model's overall significance. The *p*-value shows the probability involved with the ANOVA analysis. The parameters of the model are considered statistically significant if their *p*-values are lower than 0.05[45]. Conversely, *p*-values higher than 0.1 indicate that the parameters are not statistically significant[46]. Based on the results of this research, the y_{H_2} and y_{CO} models had significant F-values of 7713.94 and 1038.29, respectively. The *p*-values for the model term (< 0.0001) indicate that the models are significant and reliable. Between the independent variables, parameters A, B, C, AB, A^2, and C^2 for y_{H_2} and all parameters for y_{CO} are significant. The term A has the most impact on the y_{H_2} because it has the greatest value of F and the lowest value of $p >$ F. Moreover, term C, which has the greatest value of F and the lowest value of $p >$ F, has the most impact on y_{CO}. The Adeq precision signal-to-noise ratio values of the y_{H_2} and y_{CO} models are 353.2301 and 162.0399, respectively, significantly above

	y_{H_2}					y_{CO}				
	Sum of Squares	**df**	**Mean Square**	**F-value**	***p*-value**	**Sum of Squares**	**df**	**Mean Square**	**F-value**	***p*-value**
Model	6.630	9	0.7363	7713.94	< 0.0001	0.0371	9	0.0041	1038.29	< 0.0001
A-O/C	4.290	1	4.290	44,899.4	< 0.0001	0.0108	1	0.0108	2727.15	< 0.0001
B-S/C	0.1569	1	0.1569	1643.64	< 0.0001	0.0044	1	0.0044	1119.37	< 0.0001
C-T	0.0103	1	0.0103	108.07	< 0.0001	0.0198	1	0.0198	4976.15	< 0.0001
AB	0.0653	1	0.0653	684.29	< 0.0001	0.0021	1	0.0021	534.85	< 0.0001
AC	7.6e−6	1	7.6e−6	0.0801	0.7774	0.0098	1	0.0098	2480.01	< 0.0001
BC	0.0002	1	0.0002	2.020	0.1557	0.0015	1	0.0015	372.66	< 0.0001
A^2	0.2007	1	0.2007	2103.18	< 0.0001	0.0008	1	0.0008	203.36	< 0.0001
B^2	1.2e−7	1	1.2e−7	0.0012	0.9719	0.0002	1	0.0002	55.73	< 0.0001
C^2	0.0353	1	0.0353	370.27	< 0.0001	0.0006	1	0.0006	162.93	< 0.0001
Residual	0.0372	390	0.0001	–	–	0.0015	390	3.9e−6	–	–
Cor Total	6.660	399	–	–	–	0.0386	399	–	–	–

Table 6. ANOVA results for two studied responses, y_{H_2} and y_{CO}.

4. This indicates that the model developed can be used for industrial process design. Fit statistic parameters such as R^2, predicted R^2, and adjusted R^2 for the responses are listed in Table 7.

RSM Correlations

The thermodynamic data were modeled using the quadratic model equation presented in Eqs. (13) and (14). The model showed the impact and interactions of O/C, S/C, and temperature on y_{H_2} and y_{CO}.

$$\begin{aligned} y_{H_2} = {} & 0.605341 + -0.346977 \times A + -0.056851 \times B + 0.000351321 \times C + 0.020281 \times AB \\ & + 1.39033e-06 \times AC + 4.64555e-06 \times BC + 0.0415316 \times A^2 + 1.59334e-05 \times B^2 \\ & + -4.52012e-07 \times C^2 \end{aligned} \quad (13)$$

$$\begin{aligned} y_{CO} = {} & -0.000465333 + -0.00708278 \times A + -0.00805003 \times B + 0.000119038 \times C \\ & + 0.00365635 \times AB + -4.98974e-05 \times AC + -1.28554e-05 \times BC \\ & + 0.00263349 \times A^2 + 0.000688595 \times B^2 + 6.11429e-08 \times C^2 \end{aligned} \quad (14)$$

A positive value in coded equations signifies the factor that leads to optimization, while a negative value indicates an inverse link between responses and variables. The software prefers the quadratic model for the responses.

Diagnostics graphs

Diagnostic graphs are another way to determine a model's validity. As shown in Fig. 5(a,b), the quadratic models that were employed to predict the responses of y_{H_2} and y_{CO} were assessed by contrasting the predicted and actual data. The linear data distribution in Fig. 5 and the statistical parameters in Table 7 demonstrated that the quadratic models matched the thermodynamic data for both responses quite well.

Perturbation graphs

The perturbation graphs depict the impact of all parameters on response performance, with the operating midpoint range as the center point. The graphs compare the impact of all factors on y_{H_2} and y_{CO} at the center point, allowing for easy observation of each factor's impact. The perturbation scheme for comparing all operating parameters is shown in Fig. 6(a,b). y_{H_2} shows a significant drop when O/C increases, whereas S/C and temperature have a less pronounced effect. As the S/C ratio increases, y_{H_2} decreases gradually; while an increase in temperature initially results in a slight rise in y_{H_2}, it subsequently leads to a consistent reduction in y_{H_2}. Conversely, y_{CO} drops gradually as O/C and S/C increase, whereas rising temperatures show a steady rise in y_{CO}.

Statistic parameters	y_{H_2}	y_{CO}
R^2	0.9944	0.9599
Adjusted R^2	0.9943	0.9590
Predicted R^2	0.9940	0.9571
Adeq Precision	353.2301	162.0399

Table 7. The statistical parameters of the quadratic model are employed to model responses.

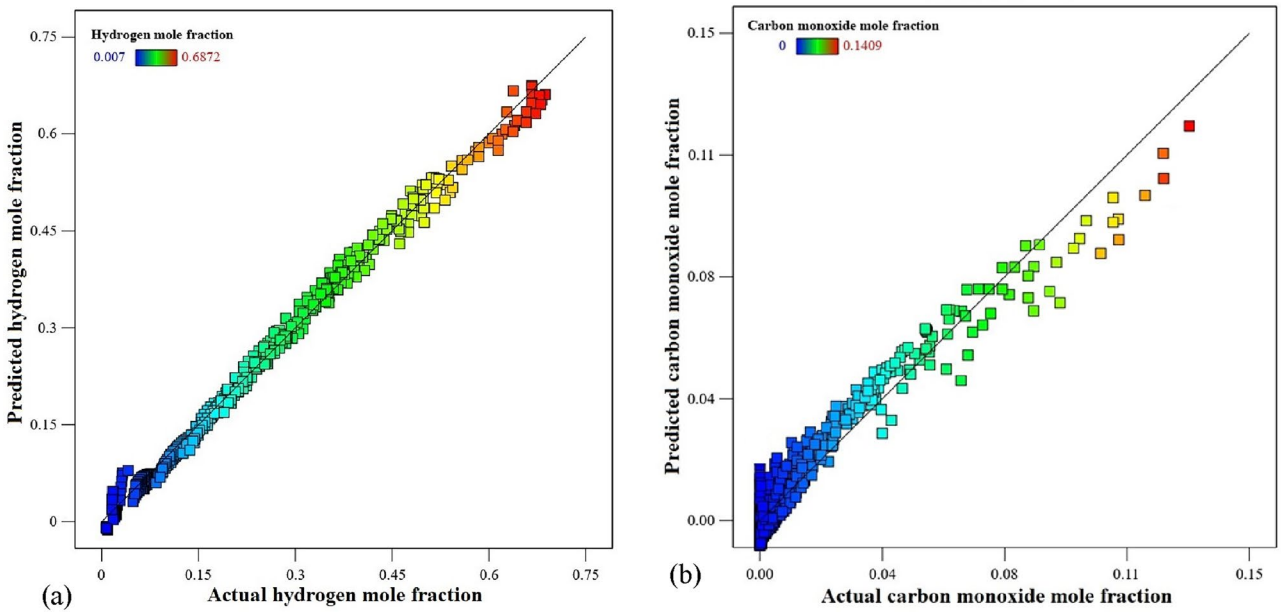

Figure 5. Predicted versus actual graphs for two responses of (**a**) y_{H_2} and (**b**) y_{CO}.

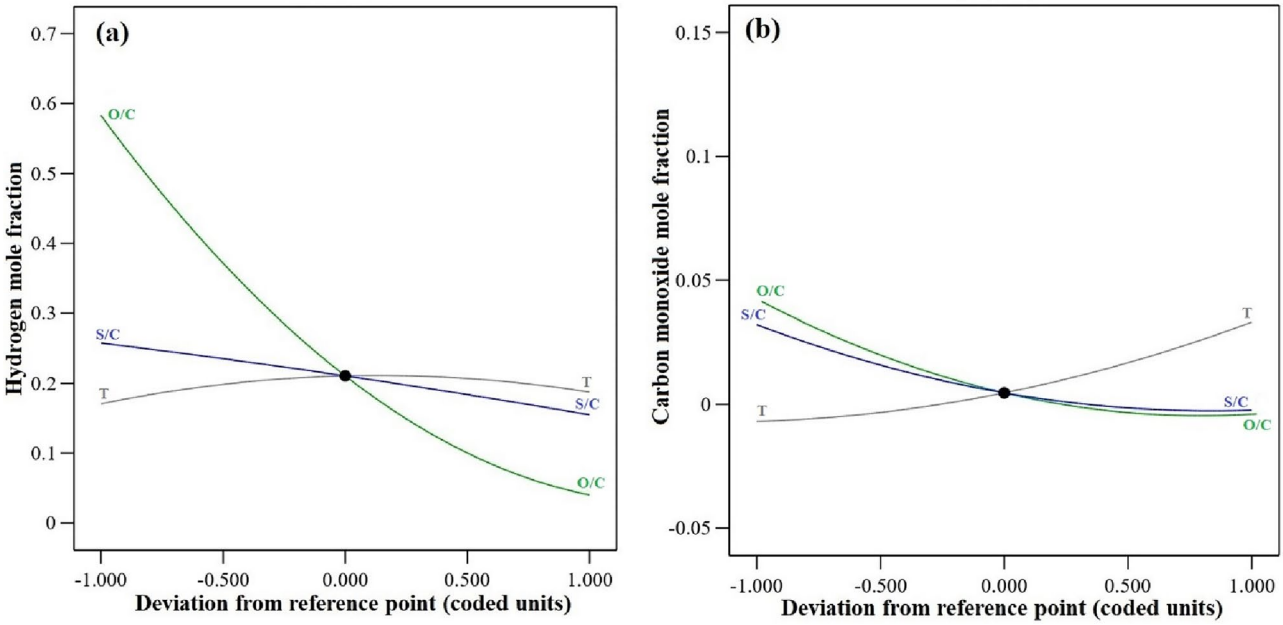

Figure 6. Perturbation graphs for (**a**) y_{H_2}, (**b**) y_{CO}.

Optimization of the hydrogen production process

The design expert software optimization tool was used to optimize the combined SR and PO processes. Therefore, to generate hydrogen-rich fuel cells efficiently, it is essential to optimize operating conditions to maximize hydrogen production and minimize CO emissions. Numerical optimization allows you to choose the preferred value for every input and response variable. In this case, the input adjustments that can be chosen are the in range, maximum, minimum, target, none (for responses), and setting an optimal response value for a specific set of conditions. In this research, the goal for all independent parameters (i.e., O/C, S/C, and T) was 'in range', and for responses, y_{H_2} was set to'maximize' and y_{CO} to'minimize'. The optimum condition with the greatest desirability is reported in Table 8.

Effect of process parameters on $\mathbf{y_{H_2}}$

The optimal condition in Table 8 was used to design three-dimensional (3D) response surface graphs. Figure 7 depicts the assessment of the interactions between independent variables and their impact on the responses.

Parameters	Goal	Lower limit	Upper limit	Optimal value
Oxygen-to-carbon ratio (O/C)	In range	0	2.8	0.4
Steam-to-carbon ratio(S/C)	In range	0.25	4	2.5
Temperature (T (°C))	In range	100	600	250
Hydrogen mole fraction (y_{H_2})	Maximize	0.007	0.7246	0.414
Carbon monoxide mole fraction (y_{CO})	Minimize	0	0.3333	0.006

Table 8. Hydrogen production optimization results using RSM.

Figure 7a indicates that pure SR (O/C = 0) conditions maximize y_{H_2}. O/C significantly affects hydrogen content owing to fuel oxidation and nitrogen dilution. Increasing O/C beyond 0.50 adds more oxygen than is required for partial oxidation, triggering full oxidation[18]. The temperature has a slight impact on the hydrogen concentration; it increases gradually up to 300 °C and then gradually decreases as the temperature rises to 600 °C because of the WGSR equilibrium. The 3D surface in Fig. 7b shows that while the temperature has a minor impact on y_{H_2}, an increase in S/C leads to a decrease in y_{H_2}, primarily due to steam dilution. Compared to the effects of steam dilution, this shift in the WGSR equilibrium toward hydrogen and CO_2 is negligible. According to the equilibrium of the WGSR, removing steam dilution increases hydrogen concentration[47]. A higher S/C suggests more steam in the system, and a higher O/C must lead to fewer CO emissions. However, as shown in Fig. 7c, due to steam dilution and fuel oxidation, the increases in O/C and S/C both result in a decrease in the end subscript. So, it is essential to use optimal values to minimize CO emissions while producing a considerable amount of hydrogen.

Effect of process parameters on $\mathbf{y_{CO}}$

As shown in Fig. 7d, the amount of CO increases with rising temperature owing to the WGSR equilibrium and reduces with increasing O/C due to the higher fraction of DME that is completely oxidized[12]. The maximum CO content occurs at O/C = 0 and the temperature of 600 °C. Figure 7e shows that as the S/C increases and the temperature decreases, y_{CO} decreases as well. By increasing the S/C, the equilibrium is shifted towards the production of CO_2 and hydrogen through the WGSR. As a result, the quantity of CO is reduced[22]. Figure 7f shows that increasing both O/C and S/C reduces CO due to more DME oxidization and shifts the WGSR equilibrium to CO_2 and hydrogen production.

ANN results

Optimizing the configuration of MLP and RBF networks

The optimum network configuration is set by trial and error by adjusting factors that impact the learning process, such as the number of neurons, training function, and activation function. Overtraining occurs when the neural network performs well exclusively on the training data but performs poorly on other domains, leading to poor precision and adaptability. It is important to reduce network running time and evaluate the model's performance using data that was not utilized for training in order to prevent overtraining.

MLP Training. The normalized data were split into three groups in order to train the MLP network: 70% of the data were randomly assigned to network training, 15% to validation, and 15% to network testing. To determine the optimal algorithm for the MLP network, three distinct training algorithms, including Levenberg–Marquardt (trainlm), Bayesian Regularization (trainbr), and Scaled Conjugate Gradient (trainscg), were examined. In order to get optimal outcomes on the test data, the configuration of the MLP network was carefully evaluated. This included the training function, the hidden layer sizes and neurons in each layer, the activation function used in each layer, and the number of epochs. Among the distinct activation functions that have been applied in this research, the sigmoid function (tansig) and linear function (purelin) have been chosen as the activation functions for the neurons in the hidden and output layers, respectively, as shown in Table 9. The outcome of several MLP configurations is shown in Table 10. The trainlm function was selected as the best approach to train the network as it performs better than all evaluated setups on all performance metrics, such as MSE, MAE, MAPE, R^2, and the number of epochs. An increase in the number of neurons and the size of the hidden layers led to a decrease in the MSE value. The MSE value was not significantly affected by increasing the number of hidden layers beyond three; therefore, in order to avoid an extended network running time, three hidden layers were considered sufficient. The optimal configuration of the MLP network was obtained with three hidden layer sizes and neuron numbers of 15, 10, and 5, respectively. The lowest MSE values and the highest R^2 were achieved. The best MSE values for y_{H_2} and y_{CO} were 3.9525e−05 and 4.8876e−05, and the best R^2 values for y_{H_2} and y_{CO} were 0.99973 and 0.99916, respectively. The details of the optimal MLP network weight matrix and bias values can be found in **Error! Reference source not found.** of supplementary. Figure 8 illustrates the regression state of the training data, validation data, testing data, and the whole dataset. The network performance throughout the training process is shown in Fig. 9a. The MLP network attained the ideal MSE validation results for nine epochs.

RBF Training. As mentioned before, every neural network consists of input, hidden, and output layers. However, the RBF neural network is distinguished by its singular hidden layer and the output of a linear function. This feedforward network variation could require a greater number of hidden-layer neurons than others. After normalizing the data, the impact of different numbers of neurons (ranging from 1 to 591) and spread values on

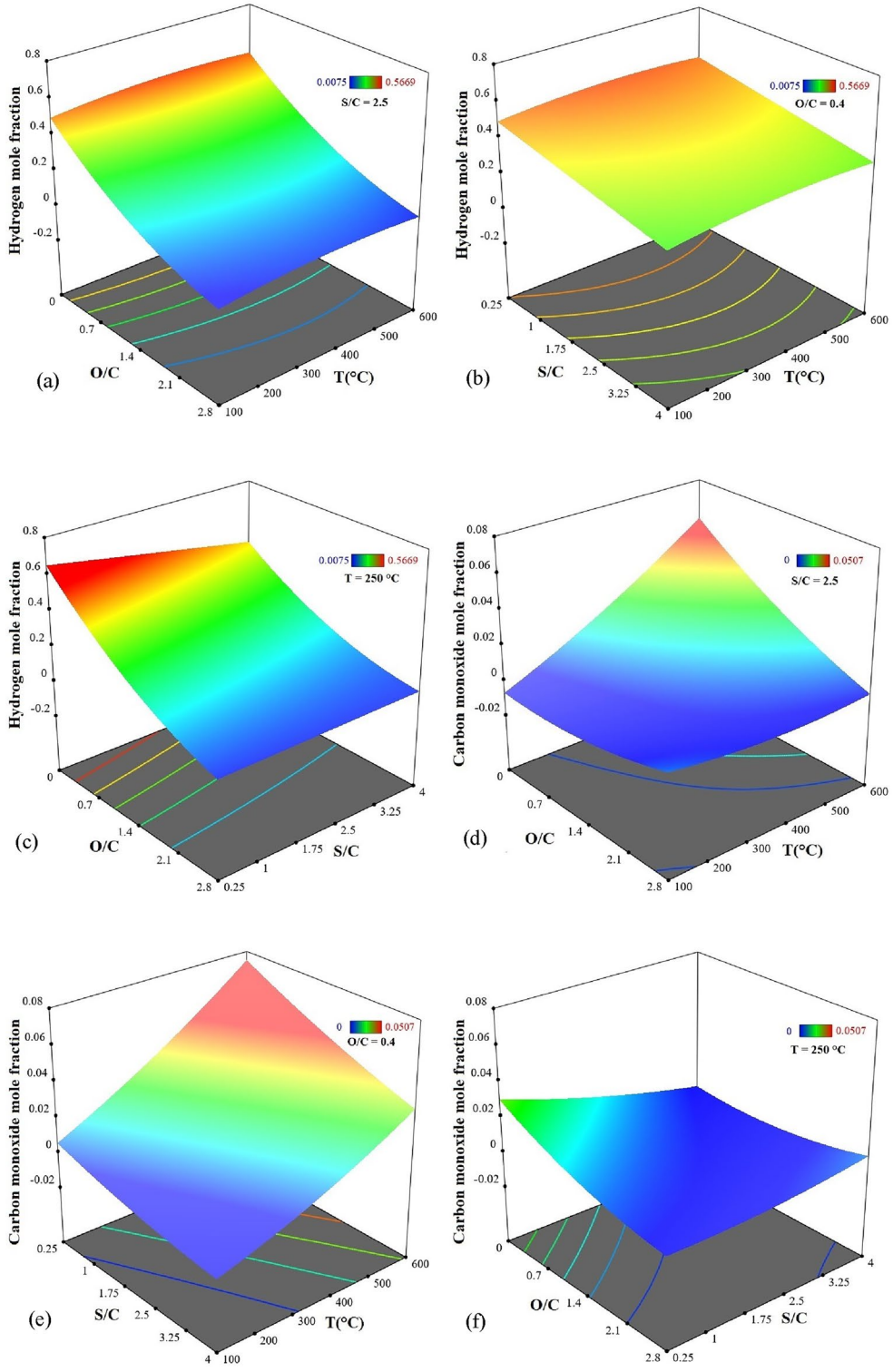

Figure 7. The 3D response surface plots showing simultaneous effects of (**a**) O/C and T on y_{H_2}, (**b**) S/C and T on y_{H_2}, (**c**) O/C and S/C on y_{H_2}, (**d**) O/C and T on y_{CO}, (**e**) S/C and T on y_{CO} (**f**) O/C and S/C on y_{CO}.

the training state of the network was studied. By setting the spread value less than one and the number of neurons to the maximum value of 591, the MSE value of the training stage was reduced significantly (almost to 0). However, this led to overtraining of the network, and the MSE value of the test data was not acceptable. Thus, the Gaussian function with a spread value of 2.5 and 80 epochs was determined to be the optimal RBF network configuration by trial and error. Where the MSE values for y_{H_2} and y_{CO} were 1.3611e−04 and 5.7466e−04, and

Mathematical algorithm function	Graph
$a = purelin(n) = n$	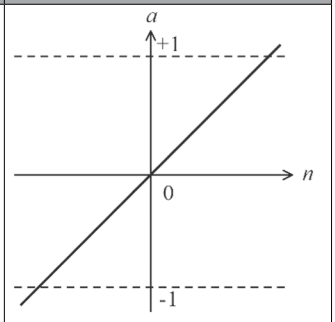
$a = tansig(n) = \frac{2}{1+e^{-2n}} - 1$	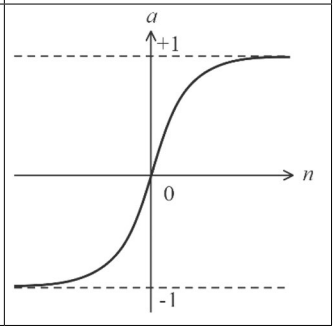

Table 9. Mathematical and graphical representations of activation functions.

Train function	Hidden layer size	MSE Train		MSE Test		22MAE Train		MAE Test		MAPE Train		MAPE Test		R^2		Epoch
		y_{H_2}	y_{CO}	y_{H_2}	y_{CO}	y_{H_2}	y_{CO}	y_{H_2}	y_{CO}	y_{H_2}	y_{CO}	y_{H_2}	y_{CO}	y_{H_2}	y_{CO}	
Trainlm	[10]	0.0011	0.0023	0.0016	0.0032	0.0231	0.0241	0.0278	0.0316	31.35	81.28	49.99	86.93	0.9925	0.9599	8
Trainlm	[10 5]	0.0009	0.0005	0.0016	0.0026	0.0191	0.0127	0.0268	0.0243	14.08	73.06	19.84	85.70	0.9944	0.9915	10
Trainlm	**[15 10 5]**	**0.00004**	**0.00005**	**0.0001**	**0.0018**	**0.0041**	**0.0036**	**0.0056**	**0.0203**	**4.53**	**19.54**	**7.08**	**22.80**	**0.9997**	**0.9992**	**9**
Trainlm	[20 15 10 5]	0.0003	2.67–4	0.0004	0.0021	0.0117	0.0077	0.0158	0.0229	14.65	103.82	24.71	76.31	0.9981	0.9955	12
Trainbr	[10]	0.0011	0.0014	0.0015	0.0037	0.0231	0.0209	0.0275	0.0344	39.65	107.84	75.88	142.28	0.9923	0.9763	16
Trainbr	[10 5]	0.0006	0.0010	0.0014	0.0043	0.0118	0.0121	0.0162	0.0215	15.05	61.43	48.42	82.85	0.9957	0.9825	18
Trainbr	[15 10 5]	0.0001	0.0003	0.0002	0.0020	0.0059	0.0081	0.0082	0.0216	7.99	28.54	9.27	45.28	0.9993	0.9949	19
Trainbr	[20 15 10 5]	0.0001	0.0002	0.0002	0.0026	0.0064	0.0061	0.0072	0.0237	8.05	31.18	8.96	48.51	0.9993	0.9972	32
Trainscg	[10]	0.0055	0.0070	0.0060	0.0141	0.0539	0.0527	0.0606	0.0682	30.76	97.16	40.07	120.33	0.9622	0.8724	45
Trainscg	[10 5]	0.0012	0.0014	0.0012	0.0034	0.0267	0.0210	0.0279	0.0320	21.65	62.27	25.38	85.81	0.9920	0.9756	90
Trainscg	[15 10 5]	0.0007	0.0008	0.0010	0.0024	0.0199	0.0160	0.0234	0.0235	20.66	48.61	24.45	73.46	0.9956	0.9862	125
Trainscg	[20 15 10 5]	0.0004	0.0004	0.0011	0.0026	0.0154	0.0125	0.0205	0.0272	14.37	34.41	21.24	81.25	0.9970	0.9933	140

Table 10. The results of several evaluated MLP training algorithms. Bold row in Table 10, represent the optimum structure of MLP.

the R^2 values for y_{H_2} and y_{CO} were 0.99908 and 0.99011, respectively. Figure 9b shows the learning curve based on the optimal topology of the RBF network.

3D response surfaces

To assess the impact of process parameters on both responses using MLP and RBF networks, data on two parameters as variables and another parameter with a constant value were given into trained networks as inputs, and y_{H_2} and y_{CO} values were computed. The 3D plots in Fig. 10(a–f) show the response surface of the best ANN configuration model under various conditions for y_{H_2} and y_{CO}. To ensure a fair comparison, the constant variables in each plot are the same as the optimal condition in RSM. Based on the results, it looks like the factors that affect both y_{H_2} and y_{CO} show the same behavior and trends as RSM.

Comparison of RSM and ANN results

Several rows of randomly chosen thermodynamic data were fed into the RSM model, MLP, and RBF networks in order to compare the outcomes of the trained networks with the model acquired by the RSM approach. The reliability of the models and networks was assessed by comparing the predicted values of y_{H_2} and y_{CO} with the actual data and computing the average absolute relative deviation (%AARD). The comparative results between

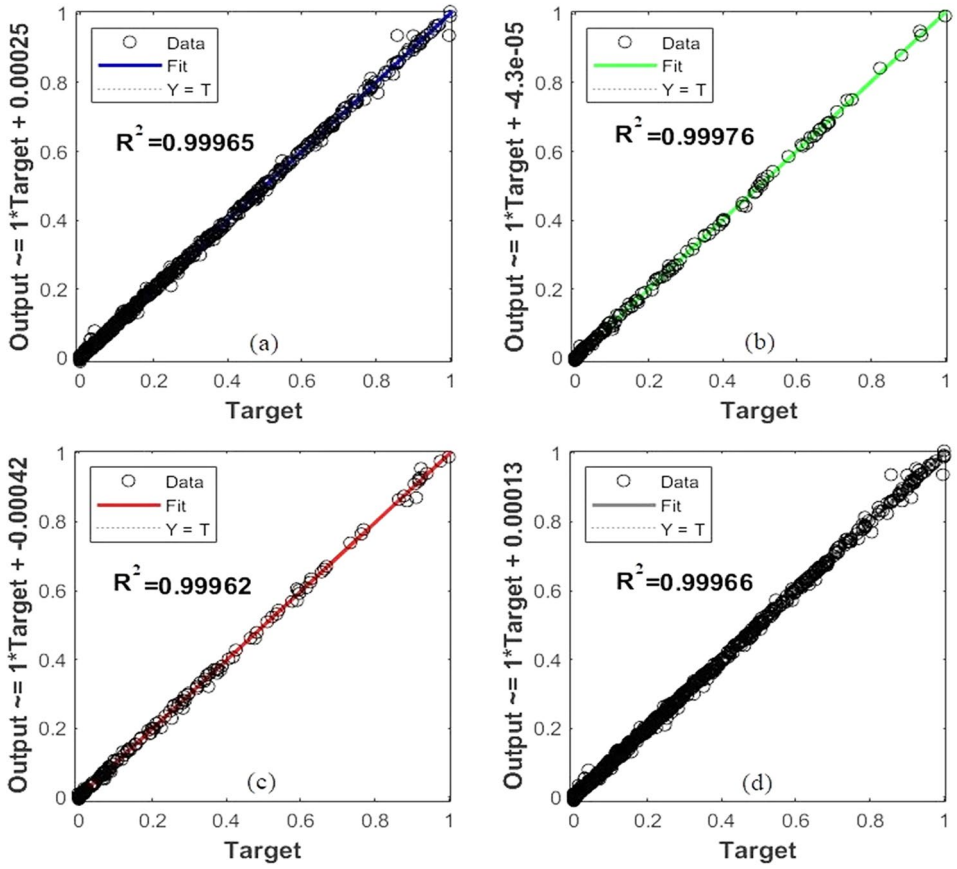

Figure 8. MLP network regression status of (a) training data, (b) validation data, (c) test data, and (d) all data for y_{H_2} and y_{CO}.

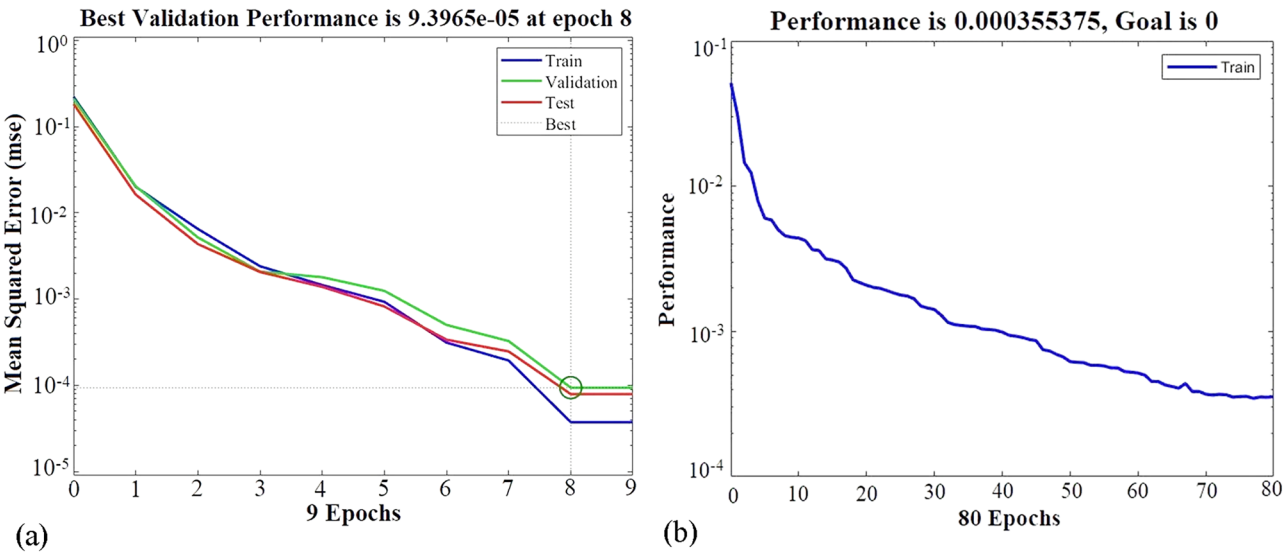

Figure 9. The MSE values during ANN training for (a) the MLP model and (b) the RBF model.

the RSM model and the ANNs are shown in Table 11. Given their developed predictability, the neural networks delivered lower %AARD values than the RSM model. Furthermore, it was determined that the MLP network outperformed the RBF network in terms of accuracy in predicting the output parameters.

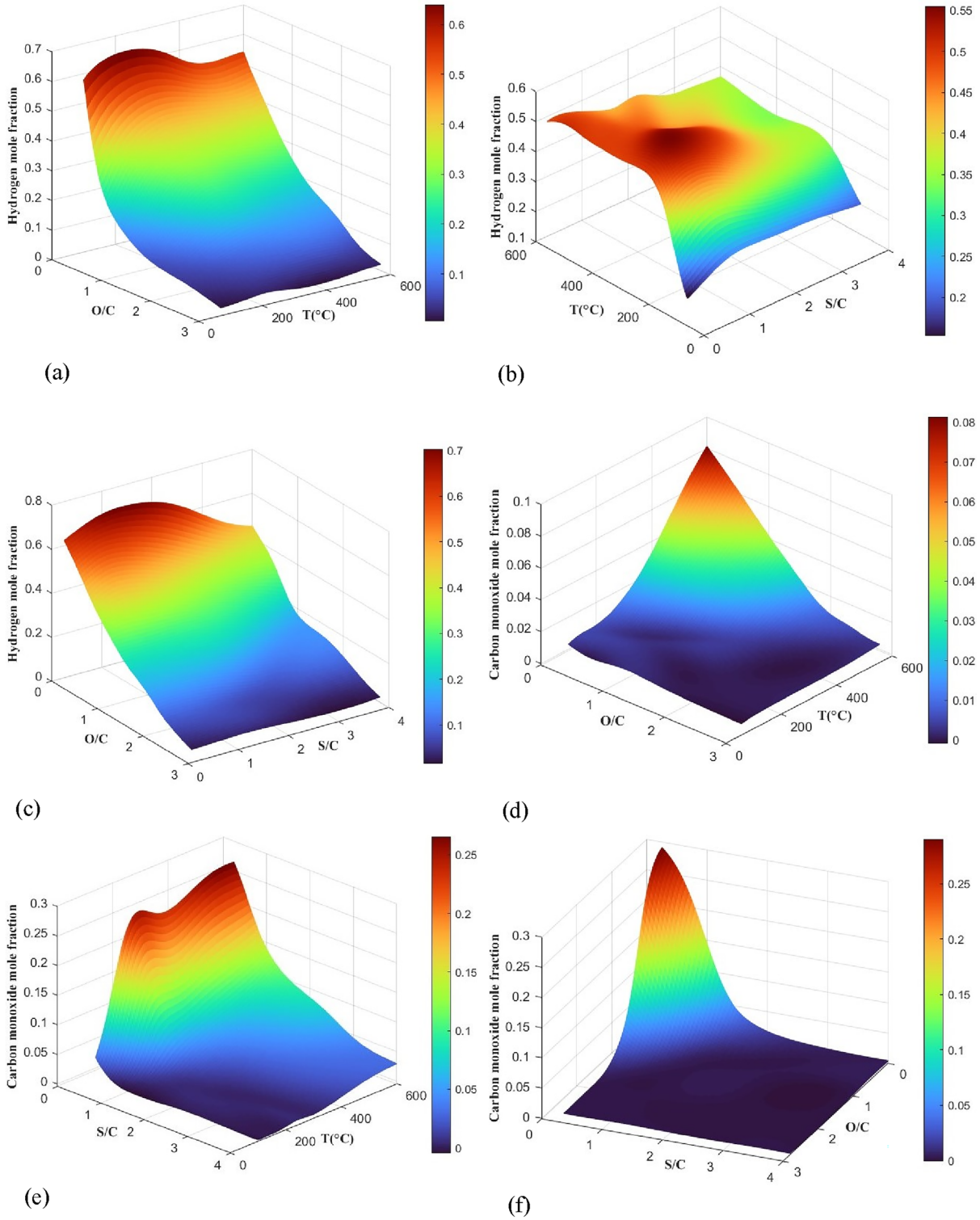

Figure 10. 3D response surface plots based on ANN by MLP model (a) O/C and T on y_{H_2}, (b) S/C and T on y_{H_2}, (c) O/C and S/C on y_{H_2}, (d) O/C and T on y_{CO}, (e) S/C and T on y_{CO}, (f) O/C and S/C on y_{CO}.

Conclusion

The rising need for analysis and process optimization, in addition to the increased accessibility of statistical software and enhanced computational capabilities, has resulted in the extensive use of Response Surface Methodology (RSM) and Artificial Neural Network (ANN) modeling tools. This research focused on analyzing the hydrogen production process factors, including the oxygen-to-carbon ratio, steam-to-carbon ratio, and temperature. The goal was to predict the responses of y_{H_2} and y_{CO} using RSM and ANN modeling methods. RSM modeling was used to assess the interaction effects of the elements under consideration. The results achieved from both

Run	(O/C)	(S/C)	T (°C)	RSM				MLP				RBF			
				y_{H_2}		y_{CO}		y_{H_2}		y_{CO}		y_{H_2}		y_{CO}	
				Y_{RSM}	AARD	Y_{RSM}	AARD	Y_{MLP}	AARD	Y_{MLP}	AARD	Y_{RBF}	AARD	Y_{RBF}	AARD
1	0.40	2.5	300	0.42	2.02	0.01	24.25	0.44	0.36	0.01	2.36	0.44	0.06	0.00	45.81
2	2.00	0.75	500	0.13	1.82	0.02	0.55	0.13	0.53	0.02	0.28	0.13	0.79	0.02	2.29
3	0	1.25	200	0.59	9.45	0.01	40.20	0.72	0.32	0.07	2.53	0.73	0.15	0.07	3.37
4	0.80	1.5	500	0.36	1.21	0.03	13.56	0.35	0.05	0.05	0.27	0.35	0.70	0.04	5.68
5	1.20	2.5	400	0.24	0.48	0.01	15.23	0.25	1.29	0.01	10.51	0.24	0.56	0.02	55.88
6	1.60	1.5	500	0.19	1.54	0.02	1.50	0.18	0.82	0.02	2.17	0.18	1.19	0.02	1.81
7	1.60	3	600	0.14	2.74	0.02	6.08	0.15	0.39	0.01	2.75	0.16	4.13	0.02	11.93
8	0.40	1.5	300	0.47	4.69	0.02	9.12	0.52	0.13	0.02	2.58	0.51	0.78	0.03	14.12
9	2.40	2.25	400	0.07	2.03	0.00	29.19	0.06	2.16	0.00	2.63	0.07	3.96	0.00	6.25
10	0.80	0.5	300	0.40	1.25	0.02	34.92	0.41	0.28	0.07	0.23	0.42	0.61	0.08	11.37

Table 11. Comparison results for several case studies conducted by MLP, RBF, and RSM.

modeling approaches exhibited a consistent and precise prediction of the thermodynamic data. In addition, the RSM used the quadratic model to establish two correlations for the responses. The optimal operating conditions for maximizing hydrogen generation and minimizing CO emissions in the combined processes of dimethyl ether steam reforming and partial oxidation were obtained at O/C of 0.4, S/C of 2.5, and temperature of 250 °C. The MLP and RBF algorithms were assessed for modeling the thermodynamic data on hydrogen generation, and their outcomes were almost identical upon comparison. After comparing the MLP algorithms, it was concluded that the Trainlm algorithm showed the greatest promise. This approach used the tansig activation function in the hidden layers and the purelin activation function in the output layer. The MLP network demonstrated superior performance in terms of mean squared error (MSE) with values of 3.9525e−05 and 4.8876e−05 for hydrogen mole fraction and carbon monoxide mole fraction, respectively, after nine epochs. On the other hand, the RBF network achieved MSE values of 1.3611e−04 and 5.7466e−04 for hydrogen mole fraction and carbon monoxide mole fraction, respectively, after 80 epochs. The hydrogen production process model, which used both ANN and RSM, achieved mean R^2 values of 0.9994 and 0.9771, respectively. Overall, the ANN method outperformed the RSM in modeling the hydrogen production process.

Data availability

The data used and analyzed during the current work is available from the corresponding author upon reasonable request.

Received: 6 April 2024; Accepted: 1 July 2024
Published online: 06 July 2024

References

1. Dawood, F., Anda, M. & Shafiullah, G. Hydrogen production for energy: An overview. *Int. J. Hydrog. Energy* **45**(7), 3847–3869 (2020).
2. Ishaq, H., Dincer, I. & Crawford, C. A review on hydrogen production and utilization: Challenges and opportunities. *Int. J. Hydrog. Energy* **47**(62), 26238–26264 (2022).
3. Nikolaidis, P. & Poullikkas, A. A comparative overview of hydrogen production processes. *Renew. Sustain. Energy Rev.* **67**, 597–611 (2017).
4. Kim, D. *et al*. Effect of γ-Al2O3 characteristics on hydrogen production of Cu/γ-Al2O3 catalyst for steam reforming of dimethyl ether. *Chem. Eng. Sci.* **216**, 115535 (2020).
5. Faungnawakij, K. *et al.* Influence of solid–acid catalysts on steam reforming and hydrolysis of dimethyl ether for hydrogen production. *Appl. Catal. A* **304**, 40–48 (2006).
6. Semelsberger, T. A., Borup, R. L. & Greene, H. L. Dimethyl ether (DME) as an alternative fuel. *J. Power Sources* **156**(2), 497–511 (2006).
7. Zhang, Q. *et al.* Hydrogen production via partial oxidation and reforming of dimethyl ether. *Catal. Today* **146**(1–2), 50–56 (2009).
8. González-Gil, R. *et al.* Hydrogen production by steam reforming of DME over Ni-based catalysts modified with vanadium. *Int. J. Hydrog. Energy* **41**(43), 19781–19788 (2016).
9. da Silva, A. L., Dick, L. F. P. & Müller, I. L. Performance of a PEMFC system integrated with a biogas chemical looping reforming processor: A theoretical analysis and comparison with other fuel processors (steam reforming, partial oxidation and auto-thermal reforming). *Int. J. Hydrog. Energy* **37**(8), 6580–6600 (2012).
10. Takeishi, K. & Akaike, Y. Hydrogen production by dimethyl ether steam reforming over copper alumina catalysts prepared using the sol–gel method. *Appl. Catal. A* **510**, 20–26 (2016).
11. Khademi, M. H., Lotfi-Varnoosfaderani, M. & Palizvan, A. Partial oxidation process for syngas production. In *Advances in Synthesis Gas: Methods, Technologies and Applications* 197–236 (Elsevier, 2023).
12. Semelsberger, T. A. *Steam reforming of dimethyl ether for generating hydrogen-rich fuel-cell feeds* (Case Western Reserve University. Springer, Cham, 2005).
13. Wang, S. *et al.* Ni-hierarchical Beta zeolite catalysts were applied to ethanol steam reforming: Effect of sol gel method on loading Ni and the role of hierarchical structure. *Mol. Catal.* **453**, 64–73 (2018).
14. Musso, M. *et al.* High performance Ni-catalysts supported on rare-earth zirconates (La and Y) for hydrogen production through ethanol steam reforming. *Charact. Assay. Catal. Today* **394**, 524–538 (2022).
15. Prasongthum, N. *et al.* Highly active and stable Ni supported on CNTs-SiO2 fiber catalysts for steam reforming of ethanol. *Fuel Process. Technol.* **160**, 185–195 (2017).

16. Lorenzut, B. *et al.* Hydrogen production through alcohol steam reforming on Cu/ZnO-based catalysts. *Appl. Catal. Environ.* **101**(3–4), 397–408 (2011).
17. Qi, C., Amphlett, J. C. & Peppley, B. A. Hydrogen production by methanol reforming on NiAl layered double hydroxide derived catalyst: Effect of the pretreatment of the catalyst. *Int. Journal of Hydrog. Energy* **32**(18), 5098–5102 (2007).
18. Semelsberger, T. A. & Borup, R. L. Thermodynamic equilibrium calculations of hydrogen production from the combined processes of dimethyl ether steam reforming and partial oxidation. *J. Power Sources* **155**(2), 340–352 (2006).
19. Pardo, E. G. *et al.* Optimization of a steam reforming plant modeled with artificial neural networks. *Electronics* **9**(11), 1923 (2020).
20. Zhang, T.-Q., Jung, S. & Kim, Y.-B. Hydrogen production system through dimethyl ether autothermal reforming, based on model predictive control. *Energies* **15**(23), 9038 (2022).
21. Chen, W.-H., et al., *Modeling and Optimization of Hydrogen Production from Methanol-Steam Reforming Using Response Surface Methodology and Artificial Neural Network*. Available at SSRN 4462603.
22. Ighalo, J. O. & Adeniyi, A. G. Thermodynamic modelling of dimethyl ether steam reforming. *Clean Technol. Environ. Policy* **23**, 1353–1363 (2021).
23. Naderi, K., Foroughi, A. & Ghaemi, A. Analysis of hydraulic performance in a structured packing column for air/water system: RSM and ANN modeling. *Chem. Eng. Process. Process Intensif.* **193**, 109521 (2023).
24. Maran, J. P. *et al.* Artificial neural network and response surface methodology modeling in mass transfer parameters predictions during osmotic dehydration of Carica papaya L. *Alex. Eng. J.* **52**(3), 507–516 (2013).
25. Amiri, M., Shahhosseini, S. & Ghaemi, A. Optimization of CO2 capture process from simulated flue gas by dry regenerable alkali metal carbonate based adsorbent using response surface methodology. *Energy Fuels* **31**(5), 5286–5296 (2017).
26. Khuri, A. I. & Mukhopadhyay, S. Response surface methodology. *Wiley Interdiscip. Rev. Comput. Stat.* **2**(2), 128–149 (2010).
27. Maran, J. P. *et al.* Box-Behnken design based statistical modeling for ultrasound-assisted extraction of corn silk polysaccharide. *Carbohydr. Polym.* **92**(1), 604–611 (2013).
28. Pashaei, H., Mashhadimoslem, H. & Ghaemi, A. Modeling and optimization of CO2 mass transfer flux into Pz-KOH-CO2 system using RSM and ANN. *Sci. Rep.* **13**(1), 4011 (2023).
29. Geyikçi, F. *et al.* Modelling of lead adsorption from industrial sludge leachate on red mud by using RSM and ANN. *Chem. Eng. J.* **183**, 53–59 (2012).
30. Kolbadinejad, S. *et al.* Deep learning analysis of Ar, Xe, Kr, and O2 adsorption on activated carbon and zeolites using ANN approach. *Chem. Eng. Process. Process Intensif.* **170**, 108662 (2022).
31. Khoshraftar, Z. & Ghaemi, A. Evaluation of pistachio shells as solid wastes to produce activated carbon for CO2 capture: isotherm, response surface methodology (RSM) and artificial neural network (ANN) modeling. *Curr. Res. Green Sustain. Chem.* **5**, 100342 (2022).
32. Hosseinzadeh, M. *et al.* Prediction of solid conversion process in direct reduction iron oxide using machine learning. *Energies* **15**(24), 9276 (2022).
33. Heidari, E., Sobati, M. A. & Movahedirad, S. Accurate prediction of nanofluid viscosity using a multilayer perceptron artificial neural network (MLP-ANN). *Chemom. Intell. Lab. Syst.* **155**, 73–85 (2016).
34. Li, G. & Shi, J. On comparing three artificial neural networks for wind speed forecasting. *Appl. Energy* **87**(7), 2313–2320 (2010).
35. Pal, S.K. and S. Mitra, *Multilayer perceptron, fuzzy sets, classifiaction*. (1992).
36. Sugumaran, V. *et al.* Efficacy of machine learning algorithms in estimating emissions in a dual fuel compression ignition engine operating on hydrogen and diesel. *Int. J. Hydrog. Energy* **48**(99), 39599–39611 (2023).
37. Moradi, M. R., Ramezanipour Penchah, H. & Ghaemi, A. CO2 capture by benzene-based hypercrosslinked polymer adsorbent: Artificial neural network and response surface methodology. *Can. J. Chem. Eng.* **101**(10), 5621–5642 (2023).
38. Zaferani, S. P. G. *et al.* Optimization of the removal Pb (II) and its Gibbs free energy by thiosemicarbazide modified chitosan using RSM and ANN modeling. *Int. J. Biol. Macromol.* **139**, 307–319 (2019).
39. Billings, S. A., Wei, H.-L. & Balikhin, M. A. Generalized multiscale radial basis function networks. *Neural Netw.* **20**(10), 1081–1094 (2007).
40. Zhang, L. & Wang, N. Application of coRNA-GA based RBF-NN to model proton exchange membrane fuel cells. *Int. J.Hydrog. Energy* **43**(1), 329–340 (2018).
41. Zhao, Z. *et al.* Prediction of interfacial interactions related with membrane fouling in a membrane bioreactor based on radial basis function artificial neural network (ANN). *Bioresource Technol.* **282**, 262–268 (2019).
42. Sharifahmadian, A., *Numerical models for submerged breakwaters: Coastal hydrodynamics and morphodynamics*. Butterworth-Heinemann. (2015)
43. Naderi, K. *et al.* Modeling based on machine learning to investigate flue gas desulfurization performance by calcium silicate absorbent in a sand bed reactor. *Sci. Rep.* **14**(1), 954 (2024).
44. Turan, N. G., Mesci, B. & Ozgonenel, O. The use of artificial neural networks (ANN) for modeling of adsorption of Cu (II) from industrial leachate by pumice. *Chem. Eng. J.* **171**(3), 1091–1097 (2011).
45. Bahmanzadegan, F. & Ghaemi, A. Exploring the effect of zeolite's structural parameters on the CO2 capture efficiency using RSM and ANN methodologies. *Case Stud. Chem. Environ. Eng.* **9**, 100595 (2024).
46. Behroozi, A. H. *et al.* Electrolyte solution of MDEA–PZ–TMS for CO2 absorption; Response surface methodology and equilibrium modeling. *Environ. Technol. Innov.* **23**, 101619 (2021).
47. Semelsberger, T. A. & Borup, R. L. Thermodynamic equilibrium calculations of dimethyl ether steam reforming and dimethyl ether hydrolysis. *J. Power Sources* **152**, 87–96 (2005).

Author contributions

Karim Mansouri: Conceptualization, Methodology, Software, Conceived and designed the experiments, Validation, Formal analysis, Investigation, Resources, Data curation, Writing-original draft, Writing-review & editing, Supervision Visualization. Fatemeh Bahmanzadegan: Conceptualization, Methodology, Software, Conceived and designed the experiments, Writing—review & editing, Validation, Formal analysis, Data curation. Ahad Ghaemi: Conceptualization, Methodology, Software, Conceived and designed the experiments, Validation, Formal analysis, Investigation, Resources, Data curation, Writing-original draft, Writing-review & editing, Supervision Visualization, Project administration Supervision, Funding acquisition, Software, Validation, Formal analysis, Investigation, Resources, Visualization.

Competing interests

The authors declare no competing interests.

Additional information

Supplementary Information The online version contains supplementary material available at https://doi.org/10.1038/s41598-024-66402-5.

Correspondence and requests for materials should be addressed to A.G.